

THE INFLUENCE OF MICROSTRUCTURE AND CARBIDE PARTICLES ON THE CREEP BEHAVIORS OF P/M ALLOYS

A.E. Segall - Washington State University-Vancouver

T Cimino, T. Murphy
Hoeganaes Corporation

T. Haberberger
Alpha Sintered Metals

B. Shaw – The Pennsylvania State University

ABSTRACT

Microstructure, related porosity, and the presence of strengthening inclusions such as carbides are known to influence the strength behaviors of PM alloys. Since an understanding of these relationships will be required if PM alloys are to be successfully used in demanding automotive applications, studies were conducted to evaluate their influence on design properties such as creep. Elevated tensile creep tests at 677^oC (1250^oF) and 35Mpa (5Ksi) were conducted to determine steady state creep rates and deformations of 434L and 304L alloys. While both materials exhibited acceptable behaviors for automotive applications, relatively large differences between creep rupture times were observed. Moreover, a large variance in the creep rupture time was observed for the 304L alloy. It is believed that the observed variations in creep behaviors between the 434L and 304L alloys can be attributed to porosity variations, the existence of a silicon oxide layer along the grain boundaries of the 304L samples, and the presence of chromium carbide within the 434L specimens.

INTRODUCTION

P/M offers many advantages for automotive applications such as net shape processing, minimal material waste during manufacturing, high volume capability with excellent part-to-part consistency, and design flexibility/weight reduction. No-doubt these advantages are behind the ongoing switch to stainless steel for exhaust systems by the major automotive manufacturers. However, increasingly strict emissions standards will result in higher operating temperatures, which will in-turn induce increasingly severe operating conditions and stresses. Moreover, the market drive for maintenance-free reliability for at least 10 years and/or 100,000+ miles will also be a significant factor in choosing the next generation of exhaust materials. Clearly, any grade of P/M alloy suitable for the next generation of exhaust system must be sufficiently robust in order to meet a long list of demanding technical and economic specifications that include: gas sealing quality, creep resistance, weldability, hot tensile and yield compressive strengths, corrosion resistance, and cost. Unfortunately, the lack of specific design properties for fatigue and corrosion, as well as the methodologies to determine them, has impeded the utilization of P/M to its full potential. Furthermore, a comprehensive methodology that determines the necessary design data, as well as investigates the often complicated interrelationships between materials properties, stress and corrosion typical of exhaust applications must be developed.

Towards these goals, a number of studies have been conducted on the elevated temperature properties of P/M stainless steel with automotive applications in-mind. Early studies[1-8] compared and contrasted the corrosion, strength, and fatigue properties of various stainless steel P/M alloys including ferritic and austenitic grades. These studies helped establish the

viability of P/M for many applications including automotive. Although efforts to determine useful elevated temperature design data for stainless P/M are still underway, there remains a significant amount of design data to be collected. To help fill this void, the study detailed in this paper represents a continuation of the efforts directed towards the development of a comprehensive database of creep behaviors of P/M austenitic and ferritic stainless steels at realistic conditions for exhaust applications.

MATERIALS STUDIED

Two candidate P/M alloys were studied for their potential application in automotive exhaust systems by virtue of their higher strength and corrosion resistance. These alloys include ferritic (434L) and austenitic (304L) grades of P/M stainless steel. In order to ensure industrially realistic and relevant tests, all specimens were manufactured on actual production equipment (when possible) to replicate full-scale production. Special attention was also given to cleanliness in the handling and processing of samples so as to avoid iron contamination and/or carbon pick-up. Moreover, attempts were made throughout specimen processing to evaluate the effects of parameter modifications on critical process-related characteristics such as density, dimensional control (which translates to tolerance control), interstitial element control (carbon, oxygen and nitrogen levels), and microstructure. Initially, each specimen was compacted at a pressure of 690 MPa (50 tsi) with the press operating in a continuous mode to simulate a normal production cycle. Following compaction, all specimens were subsequently sintered in pure hydrogen at 1290°C (2350°F) in a fully loaded furnace to realistically simulate actual production conditions. Table 1 lists the chemical composition of the two candidate alloys. Table 2 lists typical mechanical properties for the two candidate alloys.

Alloy	Fe (w/o)	Cr (w/o)	Ni (w/o)	Mn	Mo (w/o)	Cb (w/o)	C (w/o)	O ₂ (w/o)	N ₂ (w/o)
P/M 304L	Bal	18–20	8-12	2.0	–	–	< 0.03	< 0.03	< 0.03
P/M 434L	Bal	17.9	–		1.1	–	0.022	0.22	0.023

Table 1. Powder Chemical Composition for the candidate 304L and 434L stainless P/M alloys

Alloy	Sintering Temp.	Density (g/cm ³)	Ultimate (MPa)	Yield (MPa)	% Elongation
P/M 304L	1290°C (6.81	393	179	26
P/M 434 L	1290°C	7.13	345	398	14

Table 2. Typical mechanical properties for the candidate 304L and 434L stainless P/M alloys.

The microstructures of the austenitic 304L (left) and ferritic 434L (right) are shown in Figure 1. Although there is a higher degree of porosity in 304L with a corresponding lower density, the micrographs indicate that both samples show a good degree of sinter with fairly comparable grain structures. Figure 1a shows a close-up of the microstructure for the 434L alloy

illustrating the high chromium content areas within the porosity (regions A and B) and along the grain boundaries (D) as determined by the EDX.

TEST PROCEDURES AND RESULTS

A series of elevated temperature tests were conducted on the P/M 304L and 434L grades using an ARCWELD JE22 machine (currently supported by Satech Corporation, Pittsburgh PA). During the elevated temperature tests, the specimens were first allowed to heat and equilibrate at the selected temperature of 677°C (1250°F). A total of four equally-spaced thermocouples were used for each creep specimen to ensure temperature uniformity within the gauge length. After temperature equilibration, the load was slowly applied and the time dependant deformations recorded digitally at 0.1-hour increments during the steady-state period until creep rupture was observed or 1000 hours had elapsed. In order to investigate the influence of corrosion on creep rates, a number of the samples were first exposed to a corrosive environment for 120 hours in a salt-spray cabinet according to ASTM B117.

When tested at the designated 677°C (1250°F) and 35Mpa (5Ksi) temperature and stress level, respectively, the candidate alloys exhibited a number of interesting behaviors. After the constant stress was applied, there was a relatively short transient creep period where the competing effects of work hardening and annealing (recovery) are at work for both alloys. The 434L P/M alloy exhibited a somewhat unique creep behavior consisting of a short transient, period followed by a longer-term accelerated creep stage as shown in Figure 2. An average of the creep strain rates during the majority of deformation was found to be $7.8E-4 \pm 2.8E-4$ mm/mm/hr. As indicated by the relatively small standard deviation observed, the results were consistent for all of seven of the 434L specimens tested. After approximately 210 ± 52 hours, creep rupture occurred. It is in this final region of the strain-time curve where a majority of the “necking” behavior occurred. As indicated by the relatively small standard deviation observed, the creep rupture times were also consistent for all of the 434L specimens tested. Similar tests were run on P/M 434L specimens after the 120-hour exposure to a salt spray environment per ASTM B117. The negligible influence of the corrosion and the uniformity of the deformation rates between the 434L samples are also illustrated in the Weibull plot given in Figure 3. As anticipated, the corrosive environment did not influence the steady-state creep rates or the time to rupture.

When tested under the same temperature and load conditions, the P/M 304L initially exhibited distinctly different creep behaviors as also illustrated in Figures 2 and 3. After the stress was applied, there was very short transient creep region as seen in the figure. Once equilibrium was reached, a distinct and sometimes long steady-state period ensued with low strain rates of $2.8E-5 \pm 1.04E-5$ mm/mm/hr. After an average of 319 ± 435 hours of steady-state deformation, creep rupture occurred. However, unlike the 434L samples tested, no significant “necking” behavior was observed for the 304L P/M samples. More importantly, the time-to-rupture values reflect a wide range of times and an inherent variability not originally anticipated. This variability is best exemplified by the large standard deviation seen in the measured creep rupture times. The variability is also clearly illustrated in Figure 3 that shows the Weibull style plot of the creep rupture times for both alloys tested. As shown by the wide scatter and lower slope, the 304L alloys’ predictability is significantly lower than the 434L. As with the 434L corrosion tests discussed earlier, the corrosive environment induced by the salt-spray cabinet did not influence the steady-state creep rates or the time to rupture.

The SEM studies of the candidate P/M alloys indicated difference failure modes under the same creep conditions as shown in Figures 4 and 5. Examination of the 304L fracture surface shown in Figure 4 indicates a relatively undisturbed microstructure. Based on this surface, It appears intra-granular crack-growth occurred during the final creep rupture stage, as well as

during the deformation stage that preceded it. Moreover, an examination of un-etched microstructure also revealed the presence of a relatively thin silicon-oxide layer that covered fractions of the grain boundaries of some, but not all of the 304 specimens as shown in Figure 6. Interestingly, an analysis of the surface-to-volume ratio, S_v of the oxide layer (see note below) revealed that the specimens with the largest value exhibited the shortest life while the longest lasting specimen had the least as listed in Table 3.

Ranking	Time to Failure (hr)	$S_v(\text{cm}^2/\text{cc})$
1	31	67
3	51	25
5	1031+	0

Table 3. Ranking based on creep rupture time and corresponding surface-to-volume ratios measured from three of the 304L stainless P/M alloys.

Based on this analysis, it can be surmised that the brittle oxide layer weakened the grain boundary bonds and thus adversely influenced the specimens creep life. Hence, the apparent variability of the occurrence and extent of the silicon oxide may help explain the wide distribution of creep rupture times observed. At this point in time it is not understood how the silicon oxide layers formed and what controlled the extent of coverage. However, it is clear that the layers did not form as a result of the exposure to elevated temperatures during the creep tests since the longest surviving sample showed no signs of the oxide.

In contrast, the microstructure of the 434L shows no sign of the oxide layer found in the 304L samples. Moreover, the fracture surface of the 434L sample shown in Figure 5 indicates trans-granular growth occurred during the final creep rupture stage as evidenced by the rough fracture surface and indistinguishable grain structure relative to the 304L samples. One possible explanation is the presence of the chromium in the pores and more importantly, along the grain boundaries that helped strengthen or reinforce the grain boundaries. Under the tensile load, the grain boundaries were not able to slide resulting in the deformation and eventual failure of the individual grains. As with the 304L samples just discussed, there were no indications that the pre-corrosion of the samples influenced the deformation and/or failure process.

Note: The stereological method used to determine the S_v of the thin oxidized layer separating the grains was in accordance with established procedures[9] and methods. In practice, an array of parallel, horizontal lines was overlaid on an image of the unetched microstructure and single counts were made when a horizontal line crossed an oxidized boundary. The layer was treated as a thin two-dimensional film located between grains. In this way, the technique was used to determine the surface area of oxidized grain boundaries rather than the surface area of the oxide located within the boundaries. Consequently, the S_v of the oxide-covered boundaries is a fraction of the total S_v of the total grain boundary structure.

CONCLUSIONS

During tensile creep tests at a temperature of 677 °C (1250 °F) and a static stress level of 35Mpa (5Ksi), a number of interesting behaviors were observed for stainless 304L and 434L P/M alloys. For the 434L alloy, a majority of the deformation occurring in the accelerated or tertiary creep stage with a significant amount of corresponding necking. Based on an analysis of the fracture surface and microscopy, it appears that the presence of carbides along the grain boundaries effectively prohibited slip and promoted deformation within the grains. As a result, the eventual creep rupture was precipitated by transgranular crack-growth. For the 434L P/M samples tested, there was minimal scatter observed for the calculated steady-state creep rates and time of rupture. In contrast, the 304L appears to deform at a significantly lower rate with a distinct steady-state region. Interestingly, there was also wide degree of scatter observed for the time of rupture with minimal variation observed for the calculated steady-state creep rates. An examination of the fracture surfaces and microstructure indicated that the material deformed and eventually fractured along the grain boundaries. It was surmised that a brittle silicon oxide layer weakened the grain boundary bonds and thus shortened the specimens creep life for some of the 304L samples. Moreover, the possible brittle nature of the grain boundary oxide and the ensuing fracture along with the apparent variability of the occurrence of the silicon oxide may explain the wide distribution of the observed 304L creep rupture times. For both alloys tested, the pre-corrosion did not appear to adversely influence creep behavior or life.

REFERENCES

1. M.C. Baran, B.A. Shaw, A.E. Segall, H.M. Kopech, and T.E. Haberberger, "P/M Ferritic Stainless Steels for Exhaust System Components," *Transactions of the 1997, SAE International Congress and Exposition*, Detroit, MI, February 24-27, 1997.
2. M.C. Baran, A.E. Segall, B.A. Shaw, H.M. Kopech, and T.E. Haberberger, "Evaluation of P/M Ferritic Stainless Steels for Automotive Exhaust Applications," *Proceedings of the 1997, International Congress on Powder Metallurgy & Particulate Materials*, Chicago, IL, June 29-July 2, 1997.
3. Rutz, H.G., Murphy, T.F., Cimino, T.M., "The Effect of Microstructure on Fatigue Properties of High Density Ferrous Materials", *Advances in Powder Metallurgy and Particulate Materials-1996*, Vol. 4, pp 13-375 13-389, Metal Powder Industries Federation, Princeton, NJ., 1996.
4. Cimino, T.M., Rutz, H.G., Murphy, T.F., Graham, A.H., "The Effect of Microstructure on Fatigue Properties of Ferrous P/M Materials", *Advances in Powder Metallurgy and Particulate Materials-1997*, Vol. 2, pp 13-137 13-149, Metal Powder Industries Federation, Princeton, NJ., 1997.
5. Cimino, T.M., Graham, A.H., Murphy, T.F., "The Effect of Microstructure and Pore Morphology on Mechanical and Dynamic Properties of Ferrous P/M Materials", *Advances in Powder Metallurgy and Particulate Materials-1998*, Vol x, pp, Metal Powder Industries Federation, Princeton, NJ., 1998.

6. N. Nishimura, M. Ozaki, and F. Masuyama, "Effect of Dislocation Substructure on Creep Behavior of Steels Strengthened by Fine Carbides," *Key Engineering Materials*, Vol. 171-174, pp. 297-304, 2000.
7. N. Rohleder and F.G. Kollmann, "Creep Experiments for Parameter Identification of the Stochastic Model for Steck with the Powder Metallurgical Alloy AlMn10," *International Journal of Plasticity*, Vol. 6, pp. 109-122, 1990.
8. A.V. Krajnikov, A.N. Demidik, and H.M. Ortner, "Mechanical Properties and Interphase Boundary Composition of Ferritic Steels Strengthened by Yttrium and Titanium Disperse Oxides," *Materials Science and Engineering*, Vol. 234-236, pp. 357-360, 1997.
9. Underwood, E.E., *Quantitative Stereology*, Addison-Wesley Publishing Co., Reading, MA, 1970, pp. 33-34.

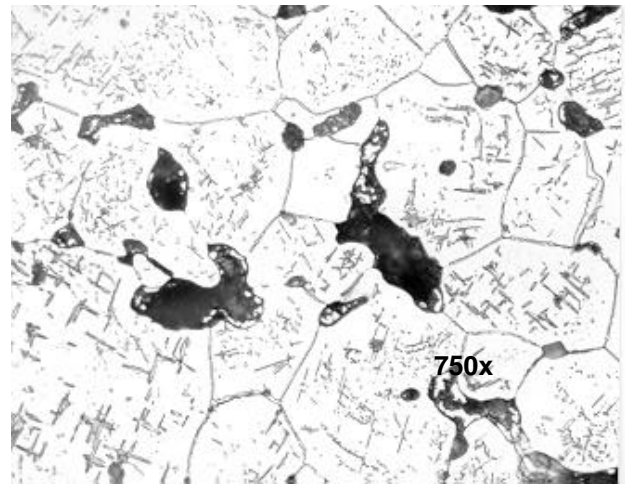
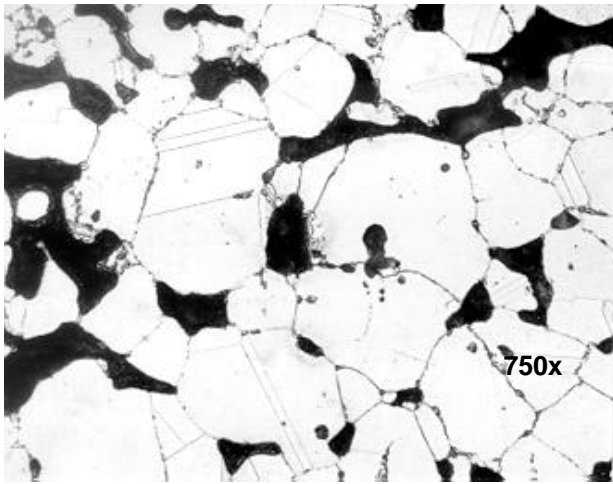


Figure 1. Microstructures for the 304L (left) and 434L (right) P/M alloys

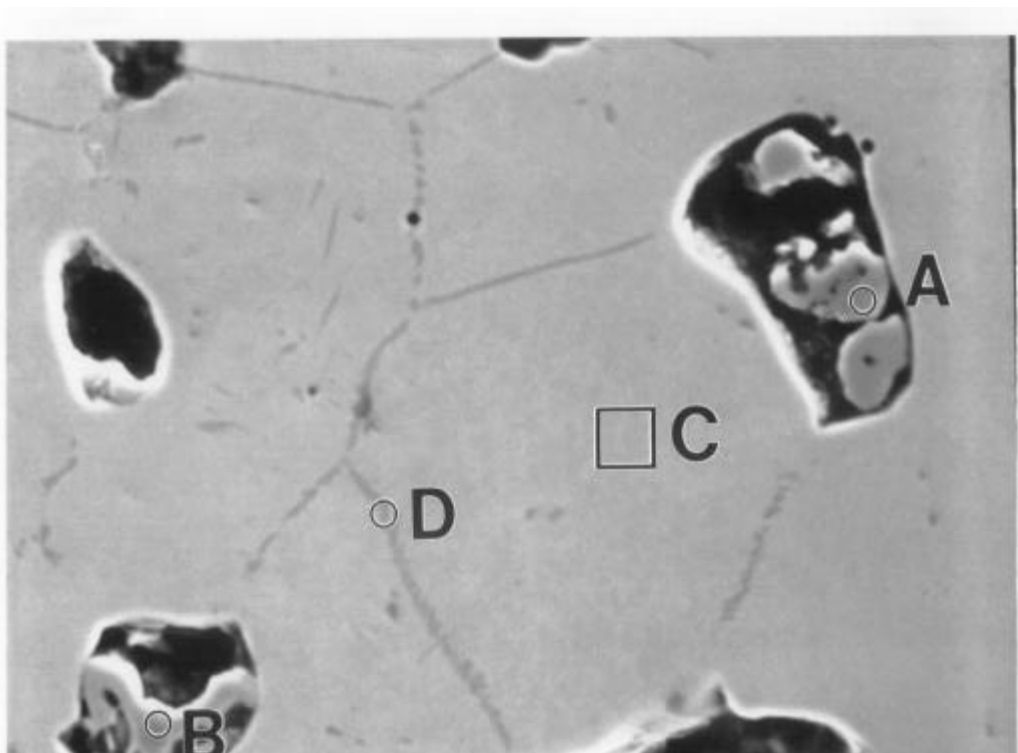


Figure 1a. Close-up of the 434L alloy microstructure showing the high chromium regions in the pores (A and B) and at the grain boundaries (D)

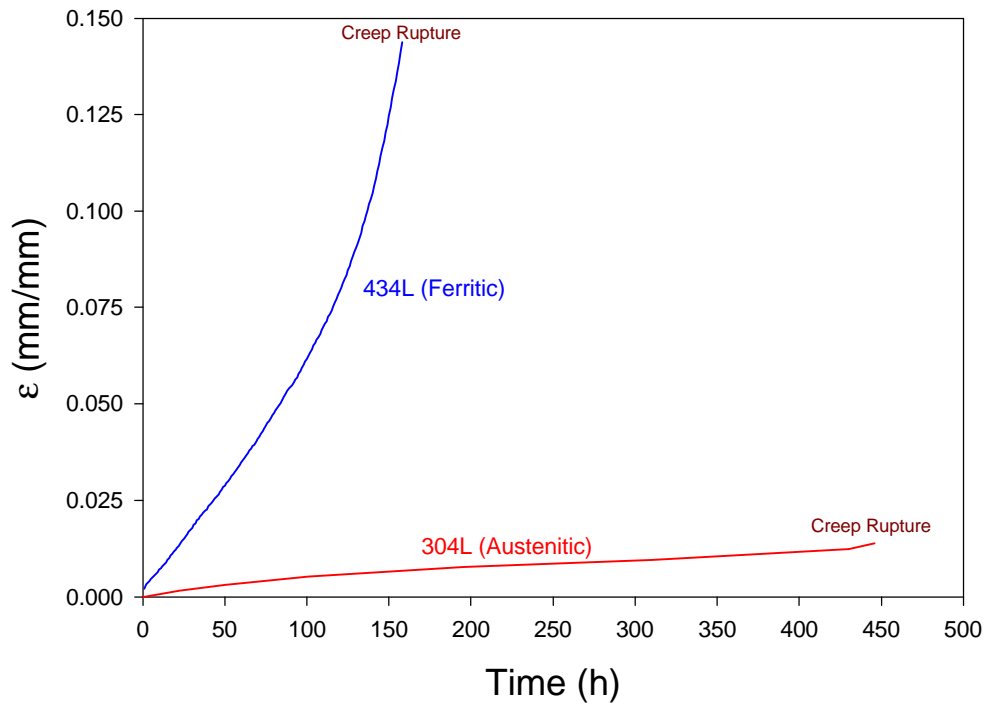


Figure 2. Typical creep strain data for measure from P/M 434L and 304 stainless steel candidate alloys at 677°C (1250°F) and 35Mpa (5Ksi).

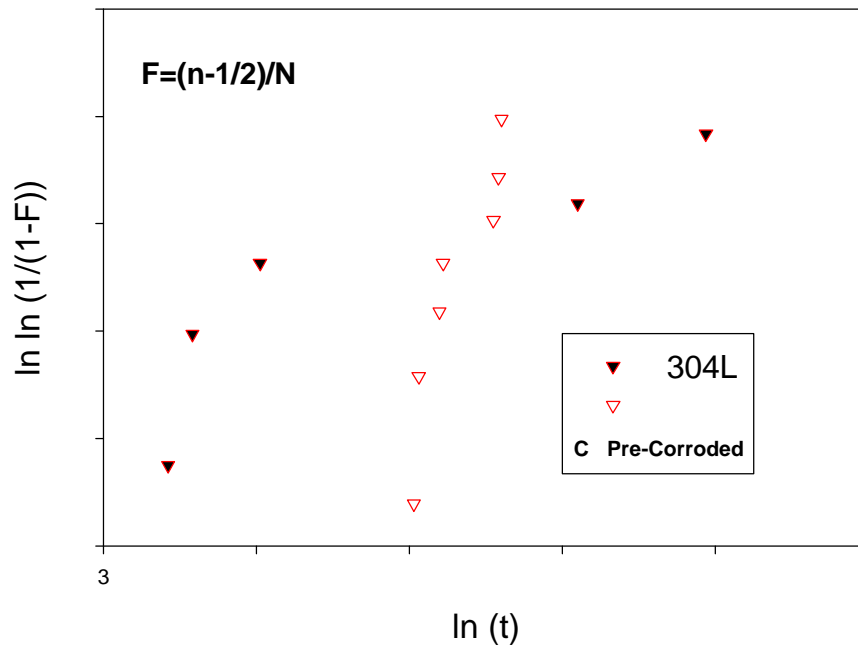


Figure 3. Weibull comparison of the measured creep rupture times for the P/M 434L and 304 stainless steel candidate alloys at 677°C (1250°F) and 35Mpa (5Ksi).

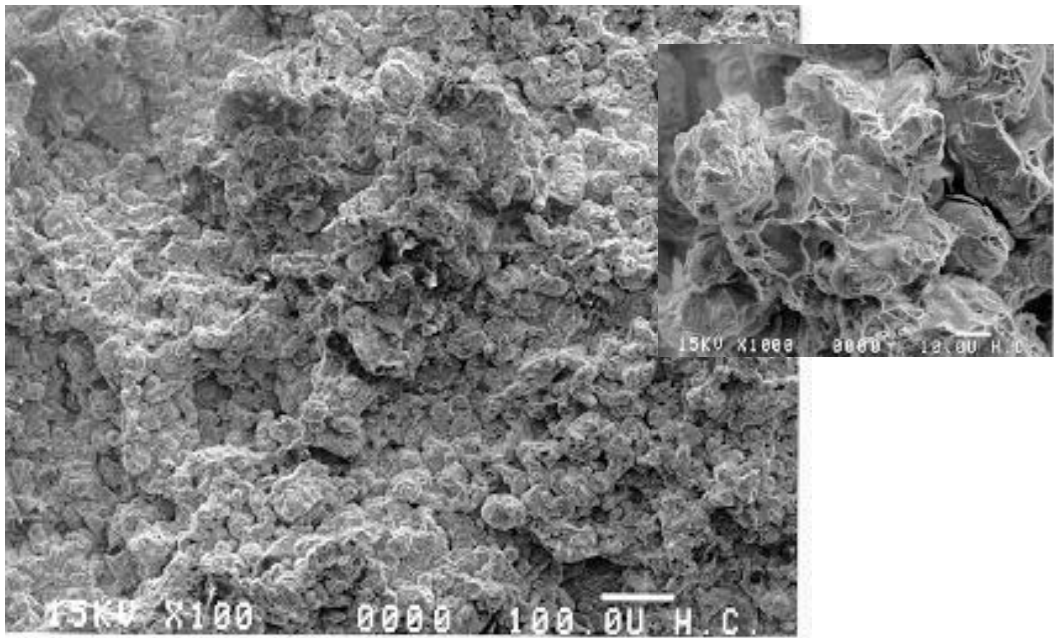


Figure 4. Fractograph of a “typical” P/M 304L stainless steel specimen after creep rupture at 677°C (1250°F) and 35Mpa (5Ksi).

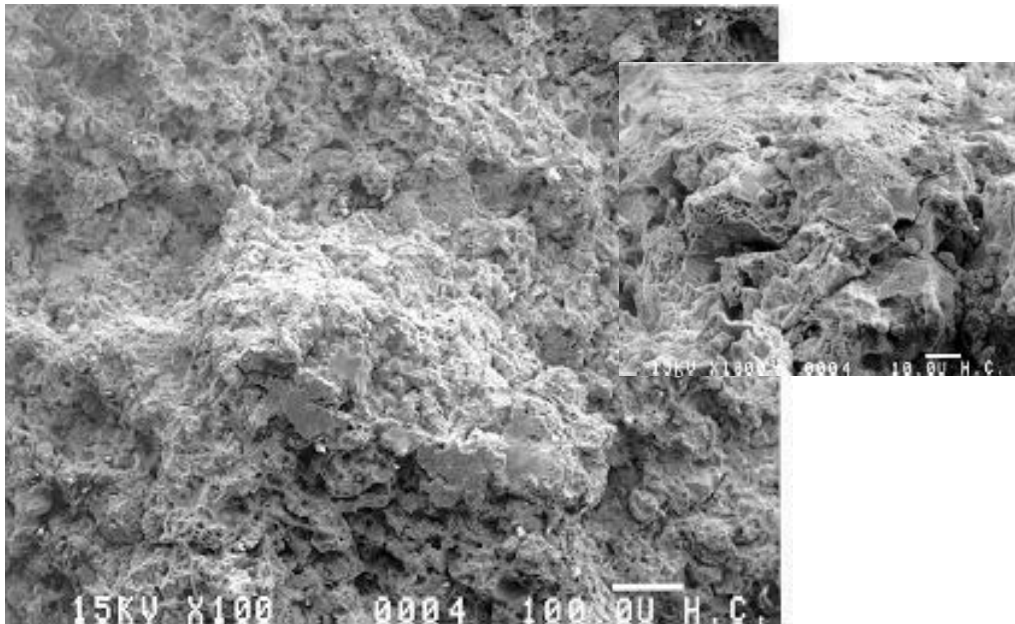


Figure 5. Fractograph of a “typical” P/M 434L stainless steel specimen after creep rupture at 677°C (1250°F) and 35Mpa (5Ksi).

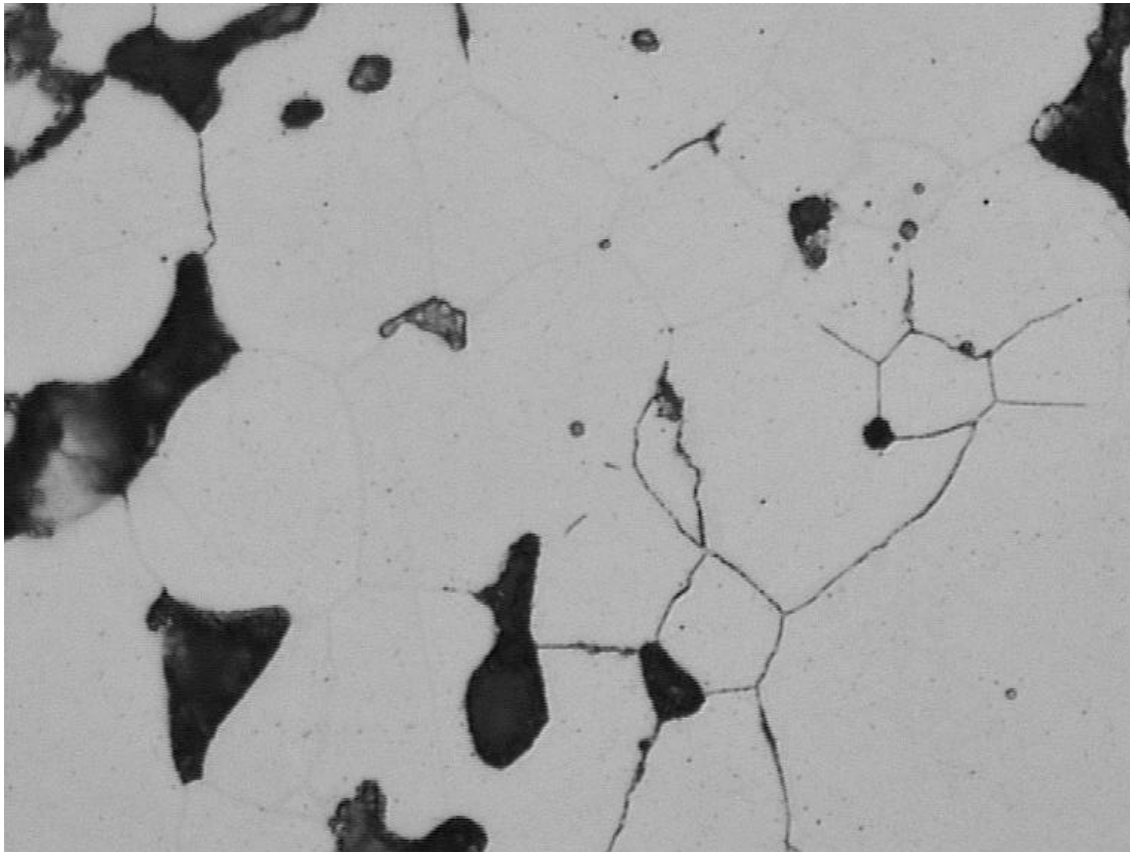


Figure 6. SEM image (1000x) showing the dark silicon oxide layer partially surrounding the grain boundaries of a 304L sample after creep rupture.